Effects of multiple ionization on the spectra of *L* x rays excited in heavy-ion collisions

V. Horvat,* R. L. Watson, and J. M. Blackadar
Cyclotron Institute and Department of Chemistry, Texas A&M University, College Station, Texas 77843-3366, USA
(Received 19 October 2007; published 28 March 2008)

Spectra of *L* x rays emitted from thick solid targets containing elements with atomic numbers ranging from 49 (In) to 67 (Ho) were measured in high resolution using a curved crystal spectrometer. The projectiles included heavy ions (Ne, Ar, Kr, and Xe) ranging in energy from 6 to 15 MeV/amu. A scaling rule was established for the apparent average fraction of *M* vacancies at the time of *L* x-ray emission and the result was compared to one obtained previously for the apparent average fraction of *L* vacancies at the time of *K* x-ray emission. The apparent degree of *L*-shell ionization at the time of *L* x-ray emission was examined as a function of target atomic number (for 6 MeV/amu Kr projectiles), projectile atomic number (for an $_{51}$Sb target), and projectile energy.

DOI: 10.1103/PhysRevA.77.032724 PACS number(s): 34.50.Fa, 32.30.Rj

I. INTRODUCTION

Multiple inner-shell ionization of an atom in heavy-ion collisions and the vacancy rearrangement that follows are fundamental processes that so far have not been adequately described in theoretical terms. The geometrical model [1] is the only fundamental theory of multiple inner-shell ionization whose results are widely available, but we found [2] that it greatly overestimates the average number of inner-shell vacancies produced in heavy-ion collisions and, therefore, cannot be relied upon for accurate predictions. However, systematic analysis of the spectra of $K\alpha$ x rays emitted from various thick solid targets under bombardment by fast heavy ions [2] has established that the apparent average fraction of *L* vacancies at the time of *K* x-ray emission, p_L^x, can be accurately described in terms of the geometrical model's universal variable X_n (for $n=2$) [1] as

$$p_L^x = a_2/[1+(b_2/X_2)^{c_2}], \tag{1}$$

where $a_2=0.537\pm0.006$, $b_2=2.11\pm0.08$, $c_2=2.02\pm0.03$, and

$$X_n = 4V[G(V)]^{1/2}Z_1 c/(nv_1). \tag{2}$$

In Eq. (2), Z_1 is the projectile atomic number, v_1 is its speed in atomic units, c is the speed of light in vacuum, n is the principal quantum number of the spectator vacancy, $V=v_1/v_2$ is the scaled projectile speed (v_2 is the average speed of an electron having principal quantum number n), and $G(V)$ is the binary encounter approximation (BEA) scaling function, as formulated by Gryzinski [3]. For simplicity, v_2 was derived from the neutral atom binding energy of L_3 electrons, as given by Deslattes *et al.* [4]. This is an important result because it provides a means of accurately predicting the characteristics of *L*-vacancy distributions for other collision systems, regardless of projectile energy, projectile atomic number, and target atomic number.

Preliminary work involving *L* x rays emitted from thick Ho targets under bombardment by 6 MeV/amu heavy ions (C, Ne, Ar, Kr, and Xe) [5] indicated that a similar dependence on X_n (for $n=3$) could describe the apparent average fraction of *M* vacancies at the time of *L* x-ray emission (p_M^x). Presented here is an extension of this work to a systematic study involving the spectra of *L* x rays emitted from a variety of thick solid targets containing elements with atomic numbers (Z_2) ranging from 49 (In) to 67 (Ho) under bombardment by 6, 10, and 15 MeV/amu heavy ions ranging in atomic number (Z_1) from 10 (Ne) to 54 (Xe). The primary objective of this work is to establish scaling rules for the spectral parameters related to the effects of multiple *L*-shell and outer-shell ionization on relative peak intensities.

A review of the previous work on the subject can be found in Refs. [2,5].

II. EXPERIMENT

Texas A&M's K-500 superconducting cyclotron was used to produce beams of Ne, Ar, Kr, and Xe ions, at 6, 10, and 15 MeV/amu. The beams were charge analyzed, collimated, and focused to a ~3 mm diam. spot onto thick solid targets oriented at 45° with respect to the beam direction. A closed circuit television system and a zinc cadmium sulfide phosphor placed in the target position were used as aides in beam focusing. During the measurements, the beam particle rate was monitored by measuring the current from the target.

Target *L* x rays were measured in high resolution using a 12.7 cm Johansson-type curved crystal spectrometer equipped with a LiF(200) crystal. The spectra were measured in the first order of diffraction with the focal circle oriented at 90° relative to the beam direction. Diffracted x rays were detected by a proportional counter filled with P-10 gas [90% Ar and 10% CH_4] flowing at the atmospheric pressure.

The targets were thick enough to stop the beam. They contained elements ranging in atomic number from 49 to 67 in the form of metallic foils (In, Sn, Sm, Tb, and Ho) or compressed pellets ($SnO_2\cdot 2H_2O$, $SnCl_2$, Sb, TeO, CsI, BaO, La_2O_3, and NdO). The latter were mixed with carbon powder to ensure conductivity. Listed in Table I is a full inventory of the combinations of beam ion species, beam energies, and target elements used in this work. Also included are those from the previous measurements with Ho [5].

*V-Horvat@tamu.edu

TABLE I. Beam species (atomic number Z_1), beam energies, and target elements (atomic number Z_2) used in this work. Also listed are the corresponding values of the universal variable X_3 [Eq. (2)], calculated based on the neutral atom binding energy of M_5 electrons [4].

Z_1	E (MeV/amu)	Z_2	X_3	Z_1	E (MeV/amu)	Z_2	X_3
6	6	67	0.51	18	6	55	1.80
10	10	67	0.76	18	6	51	1.92
10	10	65	0.77	18	6	50	1.95
10	6	67	0.85	18	6	49	1.98
10	10	51	0.90	36	10	65	2.79
10	6	62	0.91	36	6	67	3.05
10	6	56	0.98	36	6	65	3.13
10	6	55	1.00	36	10	51	3.23
10	6	51	1.07	36	6	62	3.27
10	6	49	1.10	36	6	57	3.48
18	15	67	1.22	36	6	56	3.54
18	15	62	1.27	36	6	55	3.60
18	15	60	1.29	36	6	53	3.72
18	15	51	1.39	36	6	52	3.78
18	10	65	1.39	36	6	51	3.84
18	15	49	1.41	36	6	50	3.90
18	6	67	1.52	36	6	49	3.96
18	10	51	1.62	54	10	65	4.18
18	6	62	1.63	54	10	51	4.85
18	6	60	1.68	54	10	50	4.90
18	6	56	1.77				

It has been shown previously [5] that the use of thick targets is justified in this line of work, since the effects of projectile energy loss on the spectra of L x rays emitted from the targets are small. This is because (a) most of the x rays that are produced deeper inside a target (by slower projectiles) are absorbed before they reach the detector, and (b) the projectile energy dependence of p_M^x is generally weak. Although the quantitative arguments presented in Ref. [5] referred to Ho targets, projectiles as heavy as Xe, and energies as low as 6 MeV/amu, they also hold for all the collision systems used in this work, since the effects decrease with decreasing projectile and target atomic numbers as well as with increasing projectile energy per nucleon. It was also shown in Ref. [5] that the effect of projectile energy loss on the value of the universal variable X_3 is also small (less than 5%). Furthermore, it is counteracted or possibly slightly overcompensated by calculating the average speed of M electrons based on the M_5 binding energy in neutral atoms, without taking into account increased binding due to the presence of the projectile and multiple ionization or considering the possibility of additional vacancies in the more tightly bound M subshells.

Energy calibration of the measured spectra was based on the peaks corresponding to the $L\alpha$, $L\beta_1$, and $L\beta_{2,15}$ diagram x rays of the target. These x rays originate predominantly from single-vacancy atoms in which an L-shell vacancy is produced by x rays and electrons created in collisions between the beam particles and neighboring target atoms [6–8]. Their energies were taken from Ref. [4]. The energy resolution of the spectrometer [full width at half maximum (FWHM)] was determined off-line from the spectra generated by 10 keV electron bombardment. It ranged from 6 eV (for $_{49}$In) to 27 eV (for $_{67}$Ho).

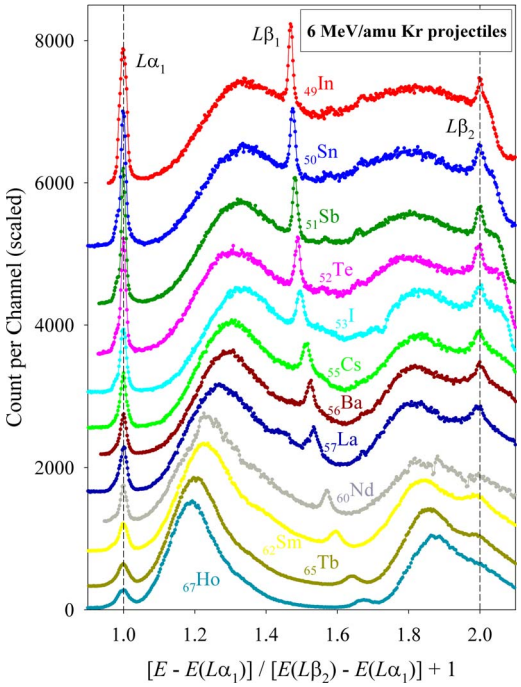

FIG. 1. (Color online) Spectra of L x rays emitted from thick solid targets (as indicated) under bombardment by 6 MeV/amu Kr ions.

III. DATA ANALYSIS

The dependence of the spectral features on target atomic number is illustrated in Fig. 1. To facilitate comparison of the spectra, the horizontal axis has been scaled such that the $L\alpha_1$ and $L\beta_2$ energies correspond to the values of 1 and 2, respectively.

Centroids of the peaks due to $L\alpha_1$ and $L\beta_2$ diagram transitions are indicated by the vertical dashed lines. The prominent narrow peak between the two corresponds to the $L\beta_1$ diagram transition. Peaks due to the other diagram transitions, such as $L\beta_3$ and $L\beta_4$, are hardly visible.

The broad distributions on the high-energy sides of the diagram peaks are due to multiple M-shell ionization caused by the projectiles. The centroid energies of these satellite distributions increase with the degree of M-shell ionization, while their widths depend mostly on the energy spread of the underlying unresolved peaks. Figure 1 shows that the diagram to satellite intensity ratio generally decreases as a function of Z_2.

The degree of M-shell ionization at the time of L x-ray emission can be described in terms of the apparent average fraction of M vacancies (p_M^x). From Fig. 1 it can be concluded that this parameter decreases as the target atomic

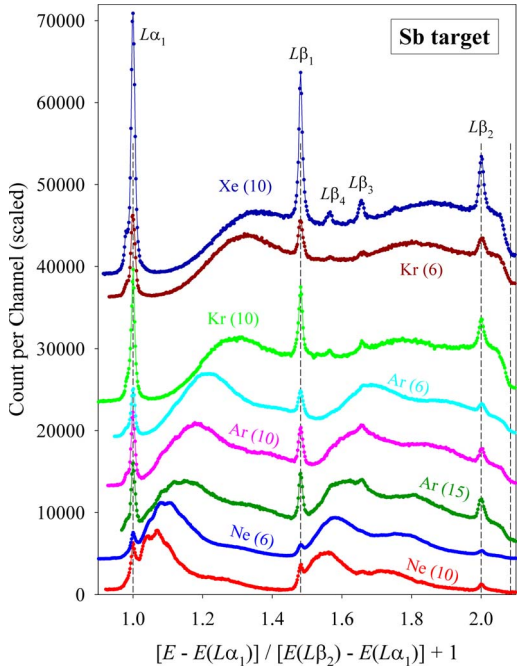

FIG. 2. (Color online) Spectra of L x rays emitted from a thick solid target of Sb under bombardment by fast heavy ions. The projectile species is indicated along with its energy in MeV/amu enclosed in parenthesis. The vertical dashed lines indicate, in order of increasing energy, the centroids of the $L\alpha_1$, $L\beta_1$, and $L\beta_2$ diagram peaks and the L_3 absorption edge.

number increases, since the centroid of the M-satellite distribution steadily shifts to lower energies as Z_2 increases. Figure 2 shows the dependence of the spectral features on projectile atomic number and energy. It is apparent from this figure that p_M^x increases with the projectile atomic number, but decreases as the projectile energy increases.

The value of p_M^x was determined from the measured spectra in a least squares curve-fitting procedure similar to that described and explained in Ref. [5]. The present procedure is set up to take into account the effects of the L_3 absorption edge. A detailed description of the fitting function used in the present work is given in the Appendix.

Two examples of the fitted spectra (those obtained with 10 MeV/amu Ne on Sb and 6 MeV/amu Kr on Sb) are shown in Fig. 3. The measured data points are shown as solid black circles, while the thick solid (red) line represents the overall fit. The background is shown as a thick dashed (gray) line, while the thin solid (pink) lines in the bottom part outline the contributions from the diagram x rays (with offset). The thin solid (green) labeled lines in the top part represent the combined contributions from all the L x-ray transitions involving h L vacancies in the initial state (i.e., the L^h components, where $h=1,2,3,\ldots$). Only for $h=1$ are individual contributions from $L\alpha_1$, $L\beta_1$, $L\beta_6$, and $L\beta_2$ x-ray satellite peaks shown in blue (thin dashed lines in the top part), while those from $L\alpha_2$, $L\beta_{15}$, $L\eta$, $L\beta_3$, and $L\beta_4$ x-ray satellite peaks are shown (with offset) in brown (thin dashed lines in the bottom part). Each individual satellite peak is due to a transition to the L shell in the presence of a specific number of spectator M vacancies. The fitting function was set to take

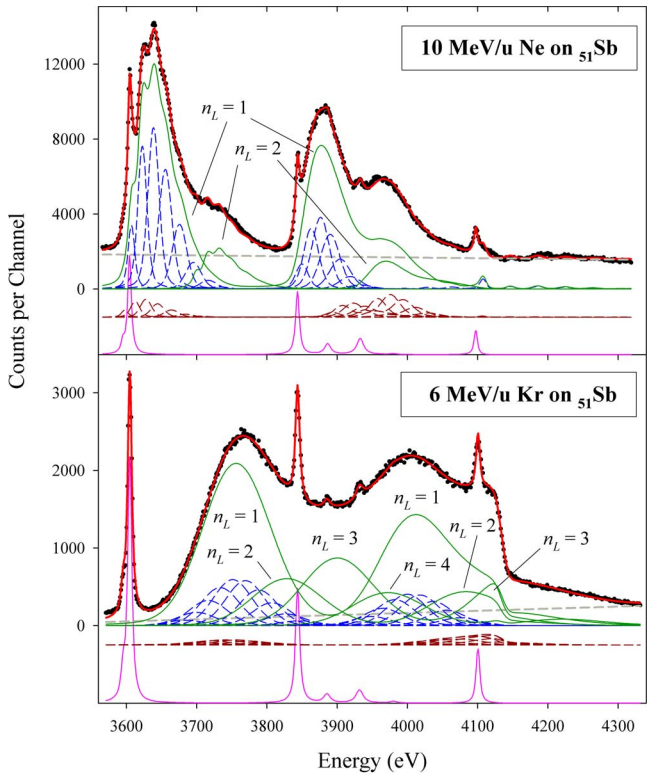

FIG. 3. (Color online) Solid circles: Measured spectra of Sb L x rays obtained under bombardment of a thick solid Sb target by 10 MeV/amu Ne (top) and 6 MeV/amu Kr ions (bottom). Lines: Overall fitting function (thick solid red) and its components (thin dashed blue (brown), thin solid green (pink), and thick dashed gray—see text).

into account the effects of the L_3 absorption edge on the x-ray peaks, but not on the background, since it was found that the background did not seem to be affected by the presence of the absorption edge.

IV. RESULTS AND DISCUSSION

A. Systematics of p_M^x

The dependence of the measured p_M^x values on the universal variable [1] is shown in Fig. 4. The solid line in Fig. 4 is a logistic curve that has been fit to the data points. It is given by

$$p_M^x = a_3/[1 + (b_3/X_3)^{c_3}], \tag{3}$$

where $a_3=0.530\pm0.012$, $b_3=1.507\pm0.044$, and $c_3=2.15\pm0.12$. The standard deviation of the residuals was found to be 0.013. Chemical effects may cause some of the deviations of the data points from the fitted curve. This assertion is supported by measurements involving the same target element in different chemical states. Specifically, Sn targets were prepared in the form of a thick metallic foil, $SnO_2\cdot 2H_2O$, and $SnCl_2$. It was found that the variations in the values of p_M^x determined from the spectra of Sn L x rays emitted from these targets under bombardment by 6 MeV/amu Kr projectiles were comparable to the residuals shown in the inset of Fig. 4.

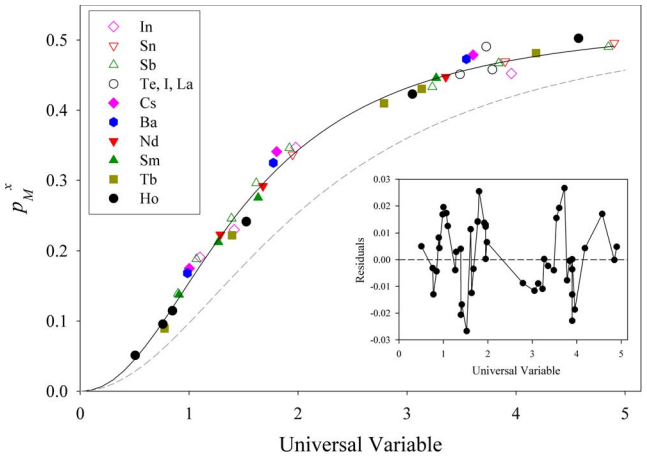

FIG. 4. (Color online) The apparent average fraction of M vacancies at the time of L x-ray emission (p_M^x) as a function of the universal variable (Table I) for various targets employed in the measurements. (Both quantities are dimensionless.) The solid line represents the best fit of a logistic curve to the data points, while the dashed line represents p_L^x as a function of X_2 [Eq. (1)]. The inset shows the residuals (i.e., the deviations of the data points from the fitted curve).

The curve representing p_M^x as a function of X_3 [Eq. (3)] lies above the one representing p_L^x as a function of X_2 [Eq. (1)]. The difference between the two sets of values reaches a maximum of 0.089 ± 0.017 at $X=1.9$. However, at large X the difference is statistically insignificant $(a_3-a_2 = 0.007 \pm 0.013)$. The maximum difference is significantly larger than the standard deviation of the residuals (0.013), which indicates that there may be some deviation from the scaling predicted by the geometrical model at the intermediate values of the universal variable. However, if the two curves are plotted as a function of X/b, the maximum difference between them is less than 0.009.

B. Effects of multiple L-shell ionization

The spectrum of Sb L x rays induced by 10 MeV/amu Ne projectiles (Fig. 3) shows L^h components for $h=1$ and 2, but there is no evidence of contributions from components having $h>2$. In contrast, the spectrum obtained with 6 MeV/amu Kr projectiles clearly exhibits L^h components with h ranging from 1 to 4.

For 6 MeV/amu Kr projectiles, the dependence of the L^h component relative intensities on target atomic number is shown in Fig. 5. Relative to the L^1 component, the L^2 component decreases in intensity as the target atomic number increases. This dependence appears to be linear. In contrast, the intensity ratio of the L^3 to L^1 component decreases much faster as a function of Z_2 and exceeds the intensity ratio of L^2 to L^1 at $Z_2<52$. The intensity ratio of the L^4 to L^1 component, on the other hand, seems to peak around the value of $Z_2=52$, where the intensity ratios L^3/L^1 and L^2/L^1 are equal.

In the spectrum shown at the bottom of Fig. 3, the L^3 component is more intense than the L^2 component. The graph shown in Fig. 5 suggests that this may be true for at least several elements having atomic number $Z_2<52$. This finding is somewhat counterintuitive, because it is expected that the cross section for h-fold L-shell ionization should monotonically decrease as h increases when there is no restriction on the impact parameter. A tentative explanation for the observed paradox might involve the effects of vacancy rearrangement between the time of L-shell ionization and L x-ray emission, combined with the h-dependence of the L x-ray fluorescence yield.

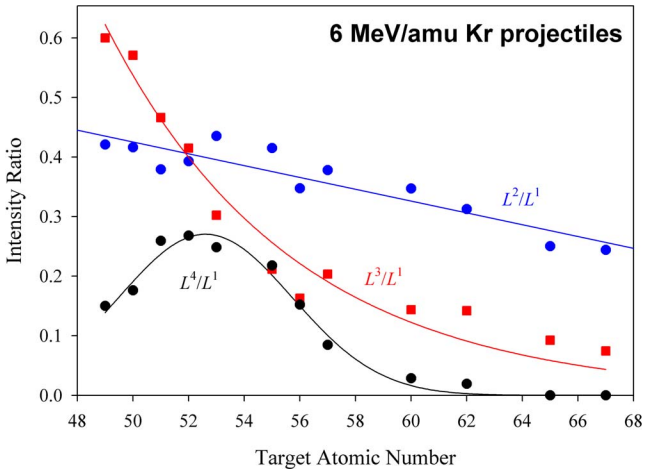

FIG. 5. (Color online) Relative intensities of the L^h x-ray components as a function of target atomic number for 6 MeV/au Kr projectiles. The lines are drawn to guide the eye.

The dependence on target atomic number of the apparent average number of L vacancies at the time of L x-ray emission ($\langle n_L \rangle$) for 6 MeV/amu Kr projectiles is shown in Fig. 6. This average value was calculated from the intensities of the L^h components. The line in Fig. 6 represents the best-fit exponential decay curve. When the projectile ion is slower than the target L electrons, the number of target L vacancies produced per collision is expected to decrease as the target binding energy (and therefore electron speed) increases. This is

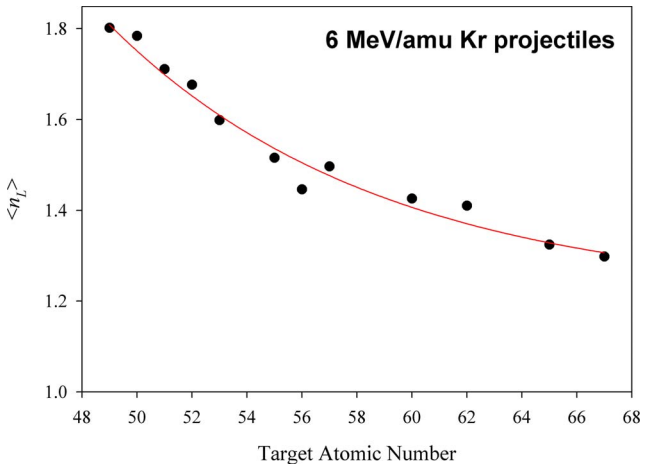

FIG. 6. (Color online) The apparent average number of L vacancies at the time of L x-ray emission as a function of target atomic number for 6 MeV/amu Kr projectiles.

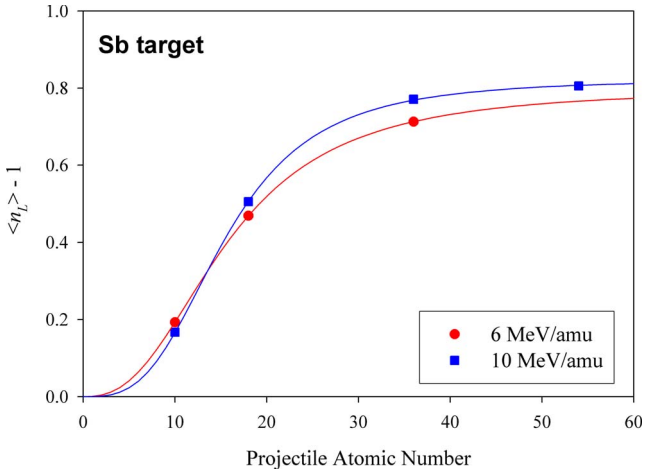

FIG. 7. (Color online) Projectile atomic number dependence of the apparent average number of spectator L vacancies at the time of L x-ray emission.

the case here. Even for the target with the smallest atomic number ($_{49}$In), the speed of the L_3 electrons (16.5 atomic units) exceeds the speed of the 6 MeV/amu Kr projectiles (15.5 atomic units). The exact dependence of $\langle n_L \rangle$ on the target atomic number has not yet been established theoretically and therefore, the fit of the exponential decay curve in Fig. 6 is strictly empirical.

The dependence on projectile atomic number of the apparent average number of *spectator* L vacancies at the time of L x-ray emission ($\langle n_L \rangle - 1$) for an Sb target is shown in Fig. 7. The blue squares and red circles represent the results of measurements with 10 MeV/amu and 6 MeV/amu beams, respectively. The lines represent best fits of logistic curves. More measurements are needed to establish whether logistic curves adequately represent the data points shown in Fig. 7 over a wider range of projectile atomic numbers and energies.

V. CONCLUSIONS

Spectra of L x rays excited in collisions involving a wide variety of thick solid targets, heavy-ion projectiles, and collision energies have been measured using a curved crystal spectrometer. The spectra were dominated by satellite structure associated with $L\alpha$ and $L\beta_1$ transitions in atoms having multiple M-shell vacancies. It was found that the measured values of p_M^x, the apparent average fraction of M vacancies at the time of L x-ray emission, defined a universal curve when plotted as a function of the geometrical model parameter X_n (for $n=3$). This curve agreed well with the ones determined previously for L x-ray emission from multiply ionized Ho atoms and was similar in shape to the one describing multiple L vacancy production in K-shell ionizing collisions. This finding adds considerable weight to the significant role the geometrical model variable plays in the description of multiple ionization by heavy ion impact.

Satellite structure associated with multiple L-shell ionization also was observed and utilized to determine $\langle n_L \rangle$, the apparent average fraction of L vacancies at the time of L x-ray emission. The dependence of this parameter on target atomic number was examined for 6 MeV/amu Kr projectiles and its dependence on projectile atomic number was established for 6 and 10 MeV/amu projectiles colliding with an Sb target. A surprising feature of the relative intensity of triple L-vacancy satellites was that it systematically exceeded the relative intensity of double L-vacancy satellites for $Z_2 \leq 52$. This might be caused by vacancy rearrangement process occurring prior to x-ray emission.

ACKNOWLEDGMENT

This work was supported by Grant No. A-0355 from the Robert A. Welch Foundation.

APPENDIX: DETAILS OF THE LEAST-SQUARES FITTING METHOD IN THE ANALYSIS OF THE SPECTRA

The fitting function y used in the analysis of the L x-ray spectra was constructed as follows:

$$y(E_i) = y_b(E_i) + y_d(E_i) + y_s(E_i) + y_h(E_i), \tag{A1}$$

where y_b, y_d, y_s, and y_h represent the background and peaks due to diagram, satellite and hypersatellite transitions, respectively. E_i is the energy corresponding to channel i. Furthermore,

$$y_b(E_i) = B_1 + B_2(E_i - E_{ini}), \tag{A2}$$

or (alternately)

$$y_b(E_i) = B_1 + B_2 \exp[-B_3(E_i - E_{ini})], \tag{A3}$$

where E_{ini} is arbitrarily chosen as the energy corresponding to the first channel in the spectral region of interest. In Eqs. (A1) and (A2), B_1, B_2, and B_3 are the parameters of the fit.

Function y_d was parametrized as follows:

$$y_d(E_i) = \eta(C_1, E_i - E_3, C_2) \sum_{j=1}^{9} \varepsilon_r(E_d^j) D^j V(\sigma_G, \sigma_L^j, E_d^j, E_i), \tag{A4}$$

where index j (in the ascending order) stands for $L\alpha_1$, $L\alpha_2$, $L\beta_6$, $L\beta_2$, $L\beta_{15}$, $L\beta_1$, $L\eta$, $L\beta_3$, $L\beta_4$, and V is a normalized Voigt function with its Gaussian width σ_G (assumed to have the same value for all j), while σ_L^j [9] and E_d^j [4] are its Lorentzian width and centroid, respectively. Parameters D^j represent peak intensities, while function η describes the step at the L_3 absorption edge at energy E_3 [4] as

$$\eta(C_1, \Delta E, C_2) = C_1 + (1 - C_1)[1 - \mathrm{erf}(\Delta E / C_2)]/2. \tag{A5}$$

The relative efficiency function ε_r was assumed to be linear,

$$\varepsilon_r(E) = 1 + C_0(E - E_d^1). \tag{A6}$$

Besides C_0, C_1, C_2, and σ_G, parameters of the fit are D^1, D^6, and D^8, while the remaining D^j's are determined from these three based on Ref. [10].

Function y_s was defined as

$$y_s(E_i) = \eta(C_1, E_i - E_3, C_2) \sum_{j=1}^{9} \sum_{k=0}^{18} \varepsilon_r(E_k^j) S_k^j V(\sigma_k^j, \sigma_L^j, E_k^j, E_i), \tag{A7}$$

where

$$\sigma_k^j = \sigma_0^j + C_3 k(18-k), \tag{A8}$$

$$\sigma_0^1 = \sigma_0^2 = \sigma_0^3 = \sigma_0^4 = \sigma_0^5, \quad \sigma_0^6 = \sigma_0^7 = \sigma_0^8 = \sigma_0^9. \tag{A9}$$

In Eqs. (A8) and (A9) the parameters of the fit are C_3, σ_0^1, and σ_0^6. The satellite peak centroids E_k^j were calculated by following the procedure described in detail in Ref. [5], except that the value of κ [Eq. (A7) of Ref. [5]] was multiplied by a correction factor C_4 (parameter of the fit) for $j=6-9$.

It was assumed that the satellite peak intensities S_k^j have the same dependence on j as do the diagram peak intensities D^j, while the dependence on k was assumed to follow a binomial distribution, i.e.,

$$S_k^j = S_{tot}^j \binom{18}{k} (p_M^x)^k (1-p_M^x)^{18-k}, \tag{A10}$$

where S_{tot}^j $(j=1,6,8)$ and p_M^x are the parameters of the fit.

Finally, the hypersatellite peaks (i.e., those corresponding to the transitions with the number of L vacancies in the initial state $h>1$) were described with

$$y_h(E_i) = \eta(C_1, E_i - E_3, C_2) \times \sum_{h=2}^{4} H_h \sum_{j=1}^{9} \sum_{k=0}^{18} \varepsilon_r[E_k^j + (h-1)\Delta E_k^j + C_5] S_k^j V[\sigma_k^j, \sigma_L^j, E_k^j + (h-1)\Delta E_k^j + C_5, E_i], \tag{A11}$$

where H_2, H_3, H_4, and C_5 are parameters of the fit, while ΔE_k^j were calculated as described in Ref. [5].

Therefore, function y, defined by Eq. (A1) has 21 or 22 variable fitting parameters: B_1, B_2, (B_3), C_0, C_1, C_2, C_3, C_4, C_5, σ_G, σ_0^1, σ_0^6, D^1, D^6, D^8, S_{tot}^1, S_{tot}^6, S_{tot}^8, H_2, H_3, H_4, and p_M^x. Each parameter affects a different feature of a spectrum, so that no significant correlation between them is expected.

[1] B. Sulik, I. Kadar, S. Ricz, D. Varga, J. Vegh, G. Hock, and D. Berenyi, Nucl. Instrum. Methods Phys. Res. B **28**, 509 (1987).

[2] V. Horvat, R. L. Watson, and Y. Peng, Phys. Rev. A **74**, 022718 (2006).

[3] J. H. McGuire and P. Richard, Phys. Rev. A **8**, 1374 (1973).

[4] R. D. Deslattes, E. G. Kessler, P. Indelicato, L. de Billy, E. Lindroth, and J. Anton, Rev. Mod. Phys. **75**, 35 (2003).

[5] V. Horvat, R. L. Watson, J. M. Blackadar, A. N. Perumal, and Yong Peng, Phys. Rev. A **71**, 062709 (2005).

[6] R. L. Watson, J. M. Blackadar, and V. Horvat, Phys. Rev. A **60**, 2959 (1999).

[7] V. Horvat and R. L. Watson, J. Phys. B **34**, 777 (2001).

[8] V. Horvat, R. L. Watson, and R. Parameswaran, Phys. Rev. A **51**, 363 (1995).

[9] J. L. Campbell and T. Papp, At. Data Nucl. Data Tables **77**, 1 (2001).

[10] S. I. Salem, S. L. Panossian, and R. A. Krause, At. Data Nucl. Data Tables **14**, 91 (1974).